EPJ Photovoltaics **16**, 18 (2025)
© T. Mochizuki et al., Published by EDP Sciences, 2025
https://doi.org/10.1051/epjpv/2025002

Available online at:
www.epj-pv.org

Special Issue on 'EU PVSEC 2024: State of the Art and Developments in Photovoltaics', edited by Robert Kenny and Gabriele Eder

ORIGINAL ARTICLE OPEN ACCESS

Performance analysis of DMF-free perovskite solar cells with vacuum quenching

Toshimitsu Mochizuki*, Shota Araki, Hidetaka Takato, and Katsuto Tanahashi

Renewable Energy Research Center, The National Institute of Advanced Industrial Science and Technology, 2-2-9 Machi-ike-dai, Koriyama, Fukushima 963-0215, Japan

Received: 30 June 2024 / Accepted: 14 January 2025

Abstract. In pursuit of perovskite solar cells compatible with silicon tandem cells, we have been exploring the vacuum quenching method. Given that N,N-dimethylformamide (DMF) is a known carcinogen in animals, we used a mixed solvent of 1-Methyl-2-pyrrolidone and Dimethyl Sulfoxide as safer alternatives. We optimized the vacuum quenching method by adjusting parameters such as annealing temperature and additives to the ink to achieve higher efficiency. We present the characteristics and structural features of solar cells in which perovskite layers were crystallized using this optimized vacuum quenching method. We fabricated a DMF-free vacuum quenched p-i-n $CsFAMAPb(I/Br)_3$ perovskite solar cell with an energy gap (E_g) of 1.69 eV and an effective area of 1.04 cm^2. We then evaluated its current-voltage characteristics using the 4-terminals method. A peak power conversion efficiency of 17.0% in the forward scan and 13.2% in the reverse scan was achieved without passivation, and 18.0% in the forward scan and 17.1% in the reverse scan by incorporating 0.5% 2-Phenylethylamine Hydroiodide (PEAI) into the perovskite ink. We measured photoluminescence spectra of perovskite crystal thin films, prepared under the same conditions as the solar cells. The photoluminescence spectra showed a consistent pattern across all samples with two gaussian components. As the conditions were optimized, the component on the high-energy side approached the intended bandgap. Furthermore, upon the addition of PEAI, the band-edge was accentuated. The XRD results indicate that the major peaks can be attributed to the cubic perovskite structure. The addition of PEAI does not significantly change the peak positions or intensities, but it reduces a minor peak attributed to PbI_2, suggesting suppressed PbI_2 precipitation. Our results indicate that the optimized conditions for vacuum quenching can produce perovskite crystals without undesirable precipitates, leading to an increase in the efficiency of solar cells.

Keywords: Green solvent / crystallization / perovskite / photovoltaics / photoluminescence / X-ray diffraction

1 Introduction

Solar cells with high power conversion efficiency (PCE) are preferred for mobile applications, despite their higher cost. This is due to the limited area for solar cell attachment and the use of expensive energy sources in vehicles and mobile devices. The efficiency of single-junction solar cells is fundamentally constrained by the Shockley-Queisser limit [1], which accounts for energy losses due to the relaxation of photoexcited carriers and radiative recombination. Even when semiconductors are free of defects that could cause Shockley-Read-Hall recombination, the maximum achievable efficiency is limited to 33.77% [2]. Furthermore, when considering Auger recombination and the range of bandgap tuning, this efficiency is further reduced to approximately 30% [3,4]. Tandem solar cells, which stack different bandgap solar cells, have experimentally achieved efficiencies over 31% by suppressing the energy that would otherwise be wasted as heat and 34.6% is reported on perovskite/Si tandem cell [5,6]. As the cost of these efficient tandem cells decreases, they are expected to meet new demand, prompting ongoing research into cost-effective production technologies. Perovskite solar cells, which are highly efficient, are primarily fabricated by repeatedly applying a solution and heat treatment or drying [7]. They are expected to become low-cost solar cells in the future. The bandgap can also be adjusted to around 1.7 eV, which is the theoretical optimal value when considering a tandem with silicon. This adjustment can be achieved by changing the recipe of the perovskite ink, making it a strong candidate for a top cell in tandem with crystalline silicon

* e-mail: toshimitsu-mochiduki@aist.go.jp

This is an Open Access article distributed under the terms of the Creative Commons Attribution License (https://creativecommons.org/licenses/by/4.0), which permits unrestricted use, distribution, and reproduction in any medium, provided the original work is properly cited.

solar cells [8,9]. To fabricate a perovskite solar cell suitable for industrial-scale silicon tandem solar cells, it's necessary to address technical challenges that do not present in the development of single-junction perovskite solar cells. In perovskite-silicon tandem solar cells, the crystalline silicon solar cells require a high PCE. When constructing a two-terminal tandem, electrical contact must be established between the bottom cell and the top cell. This implies that the surface should not be covered with an insulating film. To achieve this, using a tunnel oxidation film or a heterojunction on the surface of the bottom cell is convenient. In both scenarios, the crystalline silicon solar cell incorporates a thin film of amorphous silicon. It's known that the amorphous silicon changes its properties by annealing at approximately above 200 °C [10]. The p-i-n type perovskite solar cell, which initiates film formation from the hole transport layer (HTL), is primarily fabricated by the solution process. The substrate temperature can only be elevated up to a maximum of 150 °C. Therefore, we have been investigating p-i-n perovskite solar cells as a promising candidate for the top cell in silicon tandem configurations as the top-cell process do not damage the bottom cell. Given that silicon crystal solar cells are produced on square substrates of 156 mm or larger, it would be ideal for the perovskite top cell to be formed across the entire substrate in a single process. When using substrates of a small area, a high-quality perovskite crystal thin film can be obtained by crystallizing the perovskite ink applied to the substrate using an antisolvent method. This involves starting the crystallization by dropping an antisolvent, such as anisole, while rotating the sample with a spin coater, but it is technically difficult with large square substrates, and we are looking into the vacuum quenching method as a commercially promising method [11–15]. This is a method of starting crystallization with a rapid vacuum evacuation instead of an antisolvent, and it is expected to be compatible with the process of creating a perovskite-silicon tandem solar cell, which will be conducted on a wafer-by-wafer basis. The mixed solvent of N, N-dimethylformamide (DMF) and Dimethyl Sulfoxide (DMSO), used in perovskite ink with the antisolvent method, has also been found to be useful in the vacuum quenching method. However, DMF is a suspected human carcinogen, as it has been shown to cause cancer in animal studies [16]. Due to these concerns, DMF should be avoided in certain processes, such as the coating process in a dry booth. Therefore, we are advancing research on the use of a mixed solvent of 1-Methyl-2-pyrrolidone (NMP) [17] and DMSO. Their exposure limit is higher than that of DMF, and they also have a lower vapor pressure, making them safer alternatives. Another process suitable for large-scale applications without using antisolvents is the gas quenching method, which has been highly successful and frequently reported, including examples with NMP and DMSO mixed solvents for n-i-p type solar cell [17]. However, we are considering the vacuum quenching method because it allows for easier solvent recovery, and efficient recovery using a cold trap is expected. Additionally, the vacuum quenching method is promising because solvents are less likely to remain in the working environment and coating mechanism.

Perovskite ink with NMP and DMSO has higher viscosity and lower vapor pressure than a DMF and DMSO mixture, making it unsuitable for high-quality crystals under the same conditions. Although vacuum quenching with DMF and DMSO has been successful, similar success with NMP and DMSO has not been reported due to its lower vapor pressure. However, the properties of NMP and DMSO are beneficial for coating large substrates with a slot-die coater and crystallizing perovskite using vacuum quenching. The ink remains stable during transport, resulting in a larger process window. Therefore, establishing a process that combines the NMP and DMSO mixture with the vacuum quenching method is crucial for applications including the production of perovskite tandem solar cells using large-area bottom cells.

In the fabrication of perovskite solar cells, passivation materials are mixed into the ink or applied onto the thin film of the crystal. 2-Phenylethylamine Hydroiodide (PEAI) interacts with crystal defects and PbI_2 through PEA^+ to mitigate their effects and improve the crystal quality or reacts with PbI_2 to form a PEA_2PbI_4 2D perovskite layer on the surface of the perovskite layer, serving as a protective film. These interactions are proposed to explain the improved characteristics of perovskite solar cells when PEAI is added [18–22].

In this study, we optimized conditions such as annealing temperature and ink additives for the vacuum quenching method, with the goal of achieving high efficiency comparable to that of the antisolvent method. The 4-probe conversion efficiency reached a peak of 17.0% in the forward scan and 13.2% in the reverse scan without additive to the ink. This was observed when an area of 1.04 cm^2 was annealed at 140 °C for 2 min. By incorporating 0.5% 2-PEAInto the perovskite ink, the efficiency improved to 18.0% in the forward scan and 17.1% in the reverse scan. We will also discuss the characteristics of the perovskite thin films fabricated by this method and correlate them with the properties of solar cells, based on evaluations such as atomic force microscopy, photoluminescence measurements, and X-ray diffraction methods [23–25]. While no tandem solar cells are presented in this work, we believe that the combination of the DMF-free ink and vacuum quenching is a great candidate for applications for the tandem solar cells.

2 Materials and methods

2.1 Material formulation

The following material solutions were prepared in a dry nitrogen environment. For the formation of the hole transport layer, a 1mM solution of [2-(3,6-Dimethoxy-9H-carbazol-9-yl)ethyl]phosphonic Acid (MeO-2PACz, from Tokyo Chemical Industry, hereafter referred to as TCI) for an antisolvent sample and [4-(3,6-Dimethoxy-9H-carbazol-9-yl)butyl]phosphonic Acid (MeO-4PACz, from TCI) for the rest of the samples, was prepared in ethanol (super dehydrated, from Fujifilm Wako, hereafter referred to as Wako). As for the perovskite precursor solution, a mixture of DMF (from Wako) and DMSO (from Wako) in a volume ratio of 4:1 was used for the antisolvent method. A mixture

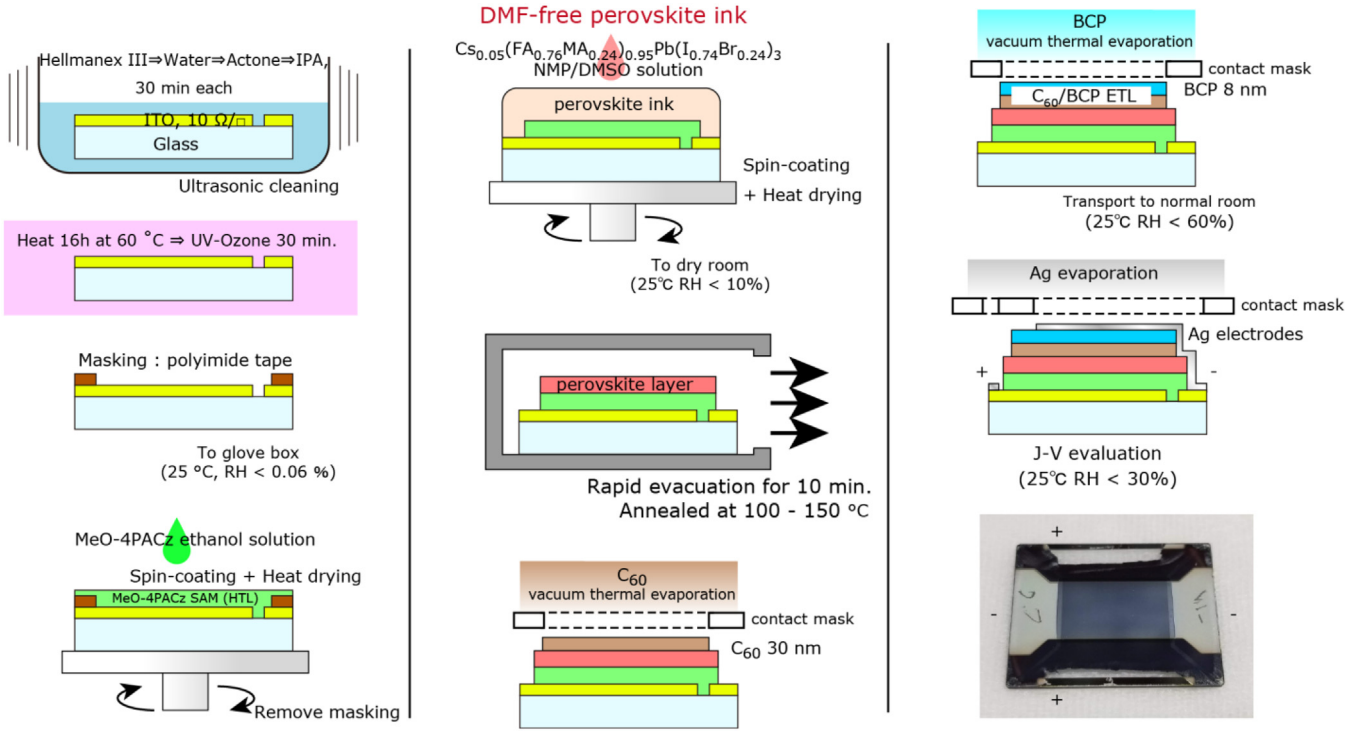

Fig. 1. Illustration of the fabrication process of vacuum quenched solar cells and picture of a sample cell.

of NMP (from Wako) and DMSO (from Wako) in a volume ratio of 19:1 was used for vacuum quenching. In these mixtures, formamidinium iodide (FAI), lead (II) iodide (PbI_2), methylammonium bromide (MABr), lead (II) bromide ($PbBr_2$) (all from TCI), and cesium iodide (CsI) (from Sigma-Aldrich) were dissolved to prepare a 1.2 M solution of $Cs_{0.05}(FA_{0.76}MA_{0.24})_{0.95}Pb(I_{0.76}/Br_{0.24})_3$ with excess Pb content. For the vacuum quenched samples, a passivation step was performed on multiple samples by mixing 0.1, 0.5, or 1 mol% of Phenethylamine Hydroiodide (PEAI, from TCI), while others were left without passivation.

2.2 Solar cell fabrication

We fabricated vacuum quenched p-i-n perovskite solar cells, along with reference samples using the antisolvent method. The samples were fabricated on glass substrates measuring $20 \times 25 \times 0.6$ mm, which were coated with a 10 ohm/sq Indium Tin Oxide (ITO) electrode. The fabrication of the vacuum quenched cells is illustrated in Figure 1. The substrate is ultrasonically cleaned for 30 min each at 40 °C with a surfactant (Hellmanex III from Hellma), pure water, acetone, and 2-propanol, and then dried overnight or longer in a clean oven at 60 °C. Just before the solution process, the surface is treated with UV ozone for 30 min, and polyimide tape is used for masking to secure the exposure area of the ITO anode for later measurement. The sample is transferred to a dry nitrogen environment and a MeO-4PACz solution is spin-coated and dried at 100 °C for 10 min to form a HTL. In the case of control samples, MeO-2PACz is used. After drying, the polyimide tape is removed, and a perovskite ink is spin coated. The sample is transferred to a dry air environment, and crystallization is initiated by quickly evacuating the sample for 10 min using a vacuum chamber with internal dimensions of 30 cm × 25 cm × 3 cm and connected to a Kashiyama Industries, Ltd.'s MU600X-020 vacuum pump with a peak pumping speed of 10000 L/min. Five seconds after starting the evacuation, the Pirani gauge attached to the vacuum chamber indicated a pressure below 10 Pa. During the 10 min of evacuation, the Pirani gauge consistently showed a pressure below 5 Pa. We fabricated a reference sample for vacuum quenching using ink with a DMF/DMSO mixed solvent. This sample was prepared using a smaller vacuum system due to the necessity of performing all operations within a glove box. The system utilized a GCD-201X oil rotary pump with an exhaust rate of 200 L/min and a cylindrical container with a diameter of 20 cm and a height of 2 cm. Crystallization is further advanced by annealing the sample for 2 or 10 min on a hot plate at 100–150 °C. For control samples, anisole is added as antisolvent during the spin-coating of perovskite ink to start crystallization and annealed for 10 min on a hot plate at 100 °C. After that, the sample is evacuated overnight, then an electron transport layer (ETL) consisting of 30 nm of C_{60} fullerene (from Sigma-Aldrich) and 8nm of Bathocuproine (BCP, from TCI) is formed by vacuum thermal evaporation, and then a cathode is formed by vacuum evaporation of silver. An example of the sample can be seen in the lower right photo of Figure 1. For the samples that are used for characterizations such as UV-Vis, XRD, and PL, the ETL is omitted.

2.3 Characterization

The characteristics of the solar cell samples were evaluated by a 4-terminal current voltage (J–V) measurement using an ADCMT 6241A DC Voltage Current Source/Monitor under AM1.5G 1sun irradiation by a two-lamp solar simulator (Sanei Electric) with a Xe lamp and a halogen lamp. The voltage sweep range was from 0 V to 1.3 V, then from 1.3 V to 0 V, and the sweep speed was set to 20 mV per second. UV-Vis transmission spectra measurements were performed with a Hitachi U-4100 Spectrophotometer. We measured the absorbance spectrum by dispersing the white light from a deuterium lamp and a halogen lamp into monochromatic light with a width of 5 nm, collimating it into parallel light with a spot size of 2 mm in diameter, and irradiating a perovskite sample. The transmitted light was collected by an integrating sphere placed just behind the sample before being measured by a photomultiplier tube and a cooled PbS sensor. The wavelength of the monochromatic light was continuously swept at a speed of 120 nm/min. Atomic-Force Microscopy (AFM) measurements were performed with a Hitachi AFM5500M. PL spectrum measurements were performed with a HORIBA Scientific FluoroMax+ Spectrophotometer by irradiating the sample with a 529 nm monochromatic light from light source consisting of a Xe lamp and a single monochromator at an incident angle of 30°. PL with emission angle of 60° was measured with detector consisting of a single monochromator and an R928P photon-counting PMT. XRD measurements were performed using a Rigaku SmartLab by evaluating the diffraction of Cu Kα radiation ($\lambda = 1.54186$ Å). The samples were scanned in the 2θ range of 5° to 60° at a step size of 0.1° and a scan speed of 5°/min with a fixed incident angle of 0.5°. The operating voltage and current were set to 45 kV and 200 mA, respectively. The diffraction was measured with a HyPix-3000 2D semiconductor sensor equipped with a beta filter.

3 Results

We optimized the fabrication conditions for solar cell samples by exploring more suitable conditions from J–V measurements and other evaluations for each sample condition. However, in this paper, we first summarize the changes in characteristics due to the crystallization conditions of vacuum quenched perovskite solar cell samples, and then compile the considerations based on evaluations under other conditions, accompanied by discussions.

3.1 Optimization of the annealing conditions without passivation

Table 1 presents the characteristics of solar cell samples without passivation crystallized under varying condition in the perovskite layer. Each row corresponds to one sample. Among these samples, the J–V curves of the ones with the highest PCE in both forward scan and reverse scan under each condition are shown in Figure 2. The solid and dashed lines represent the forward and reverse scans, respectively.

The samples prepared using the antisolvent method exhibit minimal hysteresis and have demonstrated an efficiency exceeding 18% when MeO-2PACz is used as the hole transport layer, and over 17% with MeO-4PACz. We have adjusted the conditions for the samples prepared by vacuum quenching to achieve characteristics similar to those of the antisolvent samples. However, in the samples annealed at the same temperature as the antisolvent method, the vacuum-quenched samples exhibited lower PCE compared to the antisolvent-prepared samples and showed significant inverted hysteresis with smaller current in the reverse scan. This trend was even more pronounced when using the NMP/DMSO mixed solvent compared to the DMF/DMSO mixed solvent, including unusually large hysteresis of short-circuit current in the NMP/DMSO samples annealed at 100 °C. Considering that NMP has a lower vapor pressure at room temperature and bonds more strongly to Pb^{2+} [26] compared to DMF, we hypothesized that annealing at 100 °C is insufficient for complete removal of the solvent. This could potentially slow down the crystallization process, leading to lower crystal quality, which in turn causes partially failed collection of photocarriers, resulting in the inverted hysteresis. When annealing was attempted at higher temperatures, a higher efficiency was obtained. By optimizing the annealing conditions with vacuum quenching at room temperature, annealing at 140 °C for 2 min yielded the best results, with peak efficiency of 17.0% in the forward scan and 13.2% in the reverse scan.

3.2 Optimization of passivation

We aimed to achieve efficiency close to that of the antisolvent samples by optimizing the vacuum quenching conditions. However, the absolute value was lower, and hysteresis was prominent. As will be explained later, PbI_2 is precipitated on the surface of the vacuum quenched sample. We added PEAI to the perovskite ink to suppress the precipitation. This resulted in the suppression of hysteresis and improvement of efficiency. Consequently, we obtained vacuum quenched samples at a level close to the antisolvent samples. For these samples, the vacuum quenching was followed by annealing at 140 °C for 2 min. Table 2 presents the characteristics of the samples with PEAI. Each row corresponds to one sample. Among these samples, the J–V curves of the ones with the highest PCE in both forward scan and reverse scan under each condition are shown in Figure 3. The solid and dashed lines represent the forward and reverse scans, respectively.

By mixing PEAI into perovskite ink, the hysteresis of the J–V characteristics is significantly suppressed. The V_{oc} increases as the concentration of PEAI increases, and both J_{sc} and FF reach their highest values in samples with a PEAI concentration of 0.5 mol%. As a result, the samples with a PEAI concentration of 0.5 mol% demonstrate a PCE that peaked at 18.0% and 17.1% in forward and reverse scans, respectively. This is comparable to the efficiencies of the non-passivated DMF-DMSO antisolvent samples. PCE of 17.16% (forward)/19.07% (reverse) was reported in 2017 for a combination of NMP and DMSO mixed solvents with

Table 1. Characteristics of non-passivated perovskite solar cells with varying crystallization condition.

Crystallization condition	PCE, forward/reverse (%)	J_{sc}, f/r (mA/cm^2)	V_{oc}, f/r (V)	FF, f/r (%)
Antisolvent, MeO-2PACz	18.8/18.6	19.3/19.4	1.14/1.14	81/81
Antisolvent, MeO-4PACz	18.0/17.4	18.8/16.0	1.12/1.10	74/74
	16.5/16.0	19.0/16.1	1.11/1.09	74/74
	18.0/17.3	18.9/16.7	1.11/1.09	76/74
Vacuum quenched (VQ) at 25 °C, annealed at 100 °C, 2 min.	4.6/3.5	13.1/4.1	1.08/1.05	33/84
	4.3/2.9	12.8/4.1	1.08/1.06	31/67
	4.3/2.9	13.3/3.5	1.07/1.03	30/79
	6.1/4.9	16.9/5.4	1.09/1.08	33/84
VQ at 25 °C, annealed at 100 °C, 10 min.	6.0/4.2	16.3/7.1	1.10/1.10	33/54
	4.6/2.5	13.9/4.1	1.07/1.07	31/57
	5.0/2.7	14.5/4.5	1.07/1.07	32/57
VQ at 25 °C, annealed at 100 °C, 10 min, DMF/DMSO	9.7/6.8	15.3/10.2	1.11/1.07	57/62
	10.8/9.8	18.0/13.2	1.11/1.08	55/69
	13.3/11.0	18.0/12.4	1.13/1.10	66/80
VQ at 25 °C, annealed at 130 °C, 2 min.	15.6/9.3	18.2/10.4	1.13/1.10	76/81
	14.4/8.8	18.1/9.9	1.13/1.09	70/81
	14.3/8.7	18.1/9.9	1.12/1.09	70/80
	13.9/11.4	18.4/14.3	1.07/1.06	71/75
VQ at 25 °C, annealed at 140 °C, 2 min.	16.1/12.4	18.9/14.4	1.12/1.10	76/78
	17.0/13.2	19.0/14.9	1.12/1.10	79/80
	16.4/13.1	18.9/15.0	1.12/1.10	78/80
	16.8/13.2	18.9/15.2	1.12/1.10	78/80
	16.1/12.9	18.8/14.9	1.11/1.09	77/79
	16.5/13.0	18.7/13.0	1.11/1.09	79/79
VQ at 25 °C, annealed at 150 °C, 2 min.	15.6/12.9	18.8/16.0	1.12/1.10	74/74
	15.6/12.9	19.0/16.1	1.11/1.09	74/74
	15.9/13.5	18.9/16.7	1.12/1.09	76/74

the gas quenching method [17]. Although it is an n-i-p type and has a bandgap suitable for single junctions, making direct comparison difficult, we believe our cells have room for efficiency improvement. We are currently continuing to optimize, believing that further high efficiency can be achieved through the passivation.

3.3 UV-Vis absorption spectra

In optimizing the annealing temperature, we evaluated the absorbance spectrum by measuring the UV-Vis transmission spectrum in samples without an ETL and cathode, as shown in Figure 4. All annealing was done for 2 min. The steep rise of the absorbance spectra below 750 nm correspond to the band edge of perovskite [27], and the steepest rise can be observed in the sample with a annealing temperature of 140 °C. Less sharp absorption at the band edge indicates degradation of the perovskite layer. Particularly, the duller rise at 150 °C compared to that at 140 °C suggests the decomposition of perovskite due to high-temperature annealing, so we believe that the optimal annealing temperature is around 140 °C [28].

3.4 AFM images

When the size of the perovskite film's crystalline grains is smaller than the film thickness, the PCE tends to decrease. This decrease is due to factors such as a decrease in FF caused by poor electrical conductivity at the grain boundaries, a decrease in J_{sc} due to an increase in volumes that are insulated from the surroundings, and a decrease in V_{oc} due to the effects of surface recombination [24]. as shown in Figure 5. The size of most of the crystallite is smaller than 200 nm at annealing temperatures below 130 °C. At temperatures 140 °C and above, crystallites larger than 200 nm are uncommon, and some of them are close to the thickness of the perovskite film (500 nm) used in this study. These results also suggest that there is an optimal annealing temperature around 140 °C.

3.5 PL spectra

Figure 6a shows the PL spectra of the perovskite crystal thin films on MeO-4PACz, which were vacuum quenched

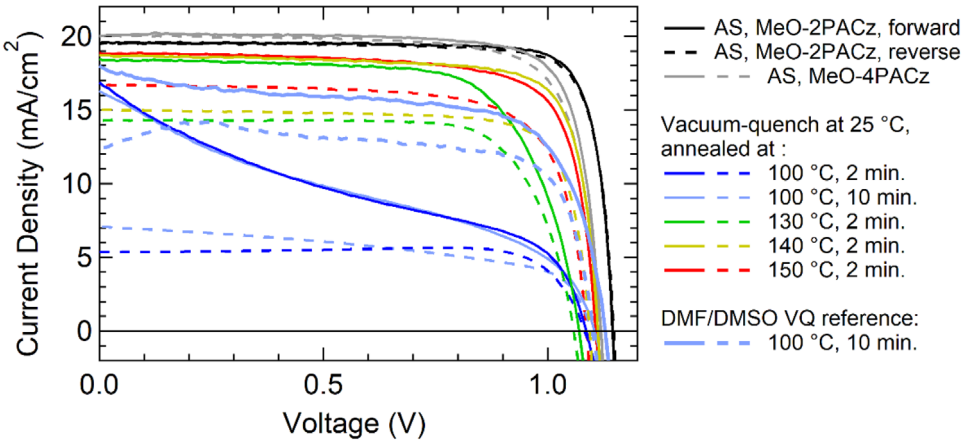

Fig. 2. *J–V* characteristics of non-passivated samples with varying crystallization condition with highest PCE among each condition.

Table 2. Characteristics of passivated perovskite solar cells with varying PEAI density.

PEAI density (mol%)	PCE, forward/reverse (%)	J_{sc}, f/r (mA/cm^2)	V_{oc}, f/r (V)	FF, f/r (%)
0.1	17.0/16.0	18.2/18.0	1.13/1.12	82/80
	17.5/16.3	18.6/18.3	1.14/1.12	82/79
	14.6/14.1	18.7/18.1	1.11/1.09	71/71
0.5	17.7/17.4	18.7/18.9	1.17/1.17	81/77
	18.0/17.1	19.1/19.2	1.17/1.16	81/77
	17.8/17.0	18.8/18.9	1.17/1.16	81/78
1.0	16.6/15.9	17.7/18.0	1.19/1.19	79/74
	16.5/15.6	17.4/17.8	1.18/1.18	80/75
	14.5/14.2	17.5/18.0	1.15/1.15	72/69

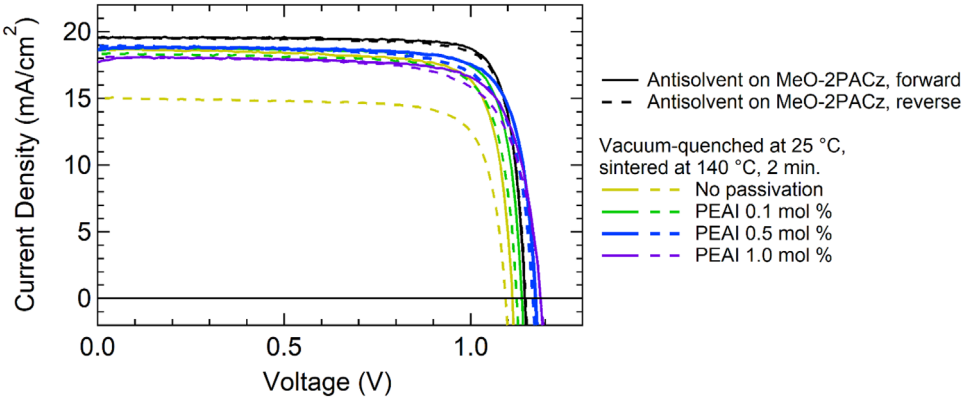

Fig. 3. *J–V* characteristics of passivated samples with highest PCE within its respective PEAI density, compared with non-passivated reference samples.

and then annealed at various temperatures, like the solar cell samples mentioned in Section 3.1. Figure 6b shows the PL spectra of the perovskite crystal thin films on MeO-4PACz, which were vacuum quenched and then annealed at 140 °C, like the solar cell sample mentioned in Section 3.2, and the perovskite crystal thin film on MeO-2PACz as a control sample. Both spectra are well fitted by two Gaussian components, as indicated by dashed lines, and their intensity and peak positions are shown in Figure 6c. Based on the reciprocity theorem, we expected that the PL intensity positively correlate with the V_{oc} of the samples [29], but this was not the case in our

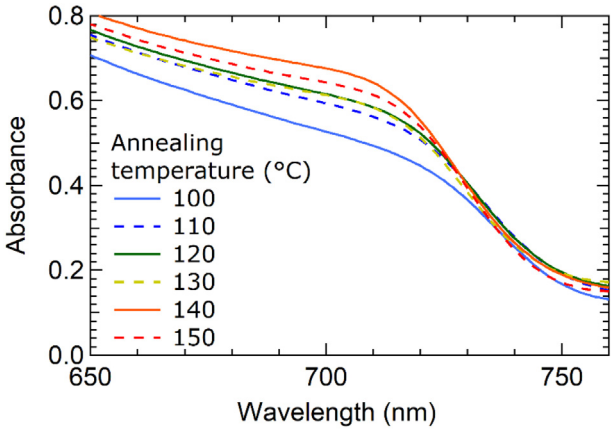

Fig. 4. Absorbance spectra of the vacuum quenched perovskite samples with varying annealing temperature.

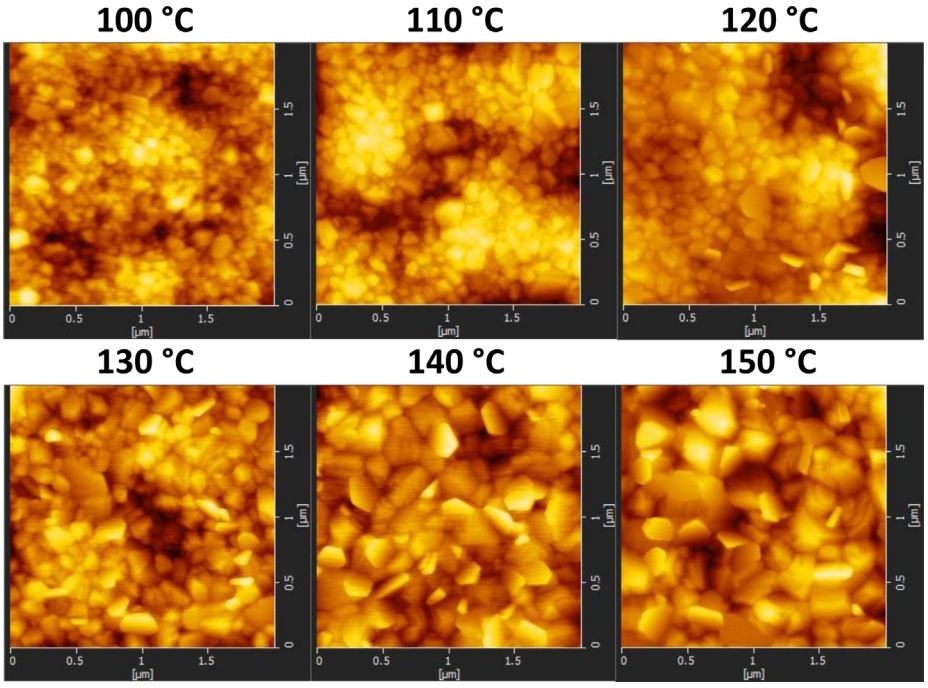

Fig. 5. AFM Images of the vacuum quenched perovskite samples with varying annealing temperature.

experiment. The peak energy also significantly shifted depending on the crystallization condition, although we expected a consistent value because the bandgap of the samples should be consistent, given that the recipe for the perovskite ink was the same. These behaviours can be interpreted as the ample part of the PL being affected by intraband emission and reabsorption. The lower energy peak is at a much lower energy than the band edge and possibly related to previously reported intraband emission from the Br precipitation region [30]. The perovskite layer measured in this study has a thickness of 500 nm. This thickness is sufficient for the redshift and deformation effects of the PL spectrum due to reabsorption of the emission to appear. For quantitative consideration, it is necessary to calculate the intrinsic PL spectrum from the absorption spectrum [31]. The UV-Vis spectrum measured in Section 3.3 has an offset in the absorption at the band edge and lower energy due to surface roughness and interference and cannot be used for accurate calculation of the intrinsic PL spectrum. Therefore, further consideration is needed.

3.6 XRD diffractogram

Figure 7 shows XRD diffractogram of the perovskite crystal thin films, which were annealed at 140 °C on MeO-4PACz with incident angle of 0.5°. Because the raw XRD data contained background originating from the ITO glass substrate, it was removed, using polynomial fitting.

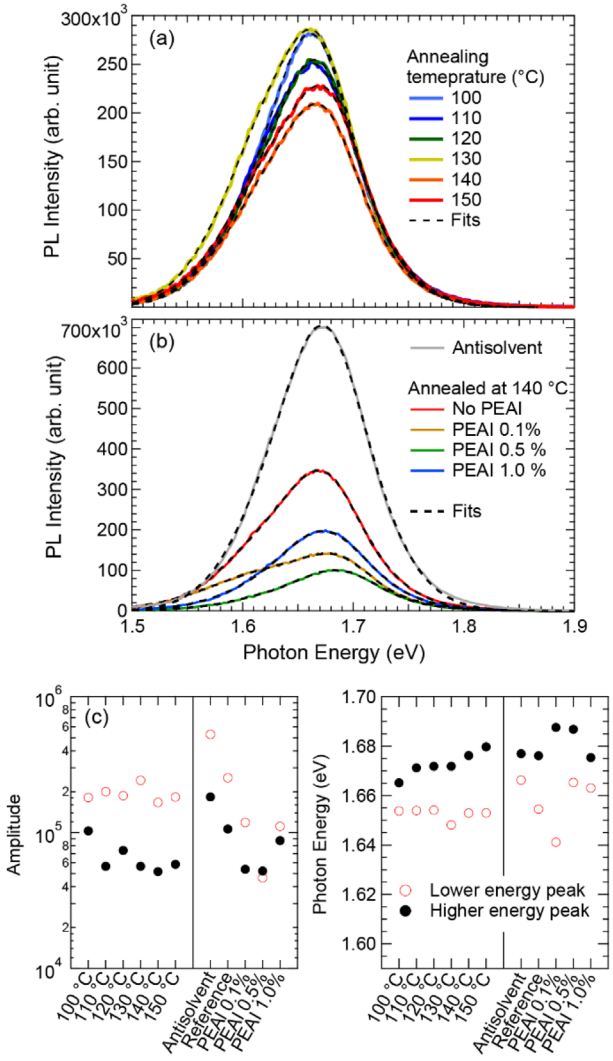

Fig. 6. Photoluminescence spectra of perovskite samples with varying crystallization conditions. (a) Photoluminescence spectra of samples similar to those described in Section 3.1, with varying annealing temperature. (b) Photoluminescence spectra of samples similar to those described in Section 3.2, with varying concentration of passivation solution. "Antisolvent" refers to the perovskite film on MeO-2PACz. (c) Peak intensity and peak position when fitting the photoluminescence spectrum with two Gaussian components.

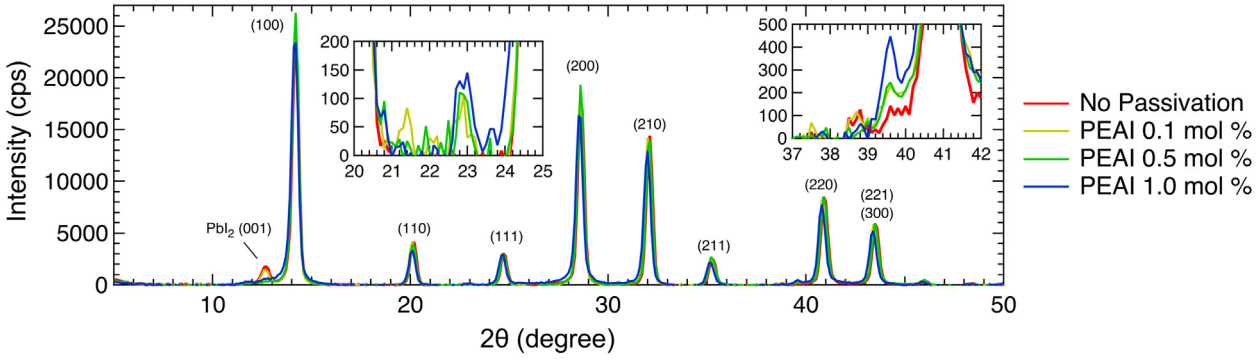

Fig. 7. XRD diffractogram of perovskite samples with varying PEAI density. The Miller indices were assigned assuming the sample to be a cubic perovskite with lattice constant close to annealed MAPbI3 (6.2758 Å)[32].

The large peak at 14.2° corresponds to (100) of cubic alpha-phase of perovskite. The small peak at 12.6° corresponds to (001) of PbI_2. In the vacuum quenched samples mixed with 0.5 mol% and 1.0 mol% PEAI, the peak of PbI_2 is insignificant, indicating that the precipitation of PbI_2 has been minimized. We believe that the high efficiency and reduced hysteresis in the solar cells made from perovskite solution mixed with PEAI through vacuum quenching are related to the suppression of PbI_2 precipitation. The prominent peaks observed in the XRD results can all be attributed to the cubic perovskite structure and are mostly consistent in peak angle and width. The small peaks unique to the passivated samples at 22.8° and 39.6°, which are shown as insets in Figure 7, are not consistent with a previous report [33], but are possibly related to 2D perovskite. A marginal decrease in the peak angle and an increase in FWHM are observed in the 1.0 mol% PEAI sample. The (200) peak angle, determined using Voigt distribution fitting, is 28.62°, 28.59°, 28.61°, and 28.54° for the samples with no PEAI, 0.1 mol% PEAI, 0.5 mol% PEAI, and 1.0 mol% PEAI, respectively. The FWHM of the same peak is 0.566°, 0.564°, 0.565°, and 0.582°. These observations suggest a slight increase in the lattice constant and a decrease in crystallite size in the 1.0 mol% PEAI sample.

4 Conclusion

We have established a method to fabricate p-i-n solar cells with perovskite ink using an NMP/DMSO mixed solvent and vacuum quenching, demonstrating efficiency comparable to those fabricated using the antisolvent method without passivation. This combination is scalable and allows for easier control of the working environment's safety. This was achieved through the optimization of conditions for solar cells and PEAI passivation. Techniques such as UV-Vis, AFM, and XRD, which have been used for the evaluation of perovskite solar cells, were also effective for the process optimization. Results from PL need further considerations. Currently, we have achieved a peak PCE of 18.0% in the forward scan and 17.1% in the reverse scan. We are aiming for higher efficiency through further optimization. Due to the scalability of this method and its compatibility with coating, we are proceeding with the production of samples on larger substrates and perovskite-Si tandem cells.

Funding

This study was supported by New Energy and Industrial Technology Development Organization, Japan, with project number JPNP20015.

Conflicts of interest

The authors have nothing to disclose.

Data availability statement

The data that support the findings of this study are available from the corresponding author upon reasonable request.

Author contribution statement

Conceptualization, H.T., S.A.; Methodology, T.M., S.A.; Software, T.M.; Validation, T.M, S.A.; Formal Analysis, T.M.; Investigation, S.A., T.M., H.T.; Resources, T.M., K.T.; Data Curation, S.A., T.M.; Writing – Original Draft Preparation, T.M.; Writing – Review & Editing, by all; Visualization, T.M.; Supervision, H.T., K.T.; Project Administration, H.T., K.T.; Funding Acquisition, H.T., K.T.

References

1. W. Shockley, H.J. Queisser, J. Appl. Phys. **32**, 510 (1961)
2. S. Rühle, Sol. Energy **130**, 139 (2016)
3. T. Tiedje, E. Yablonovitch, G.D. Cody, B.G. Brooks, IEEE Trans. Electron Devices **31**, 711 (1984)
4. J. Chantana, Y. Kawano, T. Nishimura, A. Mavlonov, Q. Shen, K. Yoshino, S. Iikubo, S. Hayase, T. Minemoto, Sol. Energy **217**, 342 (2021)
5. M.A. Green, E.D. Dunlop, M. Yoshita, N. Kopidakis, K. Bothe, G. Siefer, X. Hao, J.Y. Jiang, Prog. Photovoltaics Res. Appl. **33**, 3 (2025)
6. Longi, Solar Cell Efficiency (2024). https://www.longi.com/en/feature-report/world-record-for-solar-cell-efficiency/
7. M.A. Green, E.D. Dunlop, M. Yoshita, N. Kopidakis, K. Bothe, G. Siefer, X. Hao, Prog. Photovoltaics Res. Appl. **32**, 3 (2024)
8. S. De Wolf, E. Aydin, Science **381**, 30 (2023)
9. A. Al-Ashouri, E. Köhnen, B. Li, A. Magomedov, H. Hempel, P. Caprioglio, J.A. Márquez, A.B. Morales Vilches, E. Kasparavicius, J.A. Smith, N. Phung, D. Menzel, M. Grischek, L. Kegelmann, D. Skroblin, C. Gollwitzer, T. Malinauskas, M. Jošt, G. Matič, B. Rech, R. Schlatmann, M. Topič, L. Korte, A. Abate, B. Stannowski, D. Neher, M. Stolterfoht, T. Unold, V. Getautis, S. Albrecht, Science **370**, 1300 (2020)
10. R. Street, J. Kakalios, C. Tsai, T. Hayes, Phys. Rev. B **35**, 1316 (1987)
11. J. Silvano, J. Sala, T. Merckx, Y. Kuang, P. Verding, J. D'Haen, T. Aernouts, B. Vermang, W. Deferme, EPJ Photovolt. **13**, 12 (2022)
12. L. Gu, F. Fei, Y. Xu, S. Wang, N. Yuan, J. Ding, ACS Appl. Mater. Interfaces **14**, 2949 (2022)
13. Y. Xu, C. Zhou, X. Li, K. Du, Y. Li, X. Dong, N. Yuan, L. Li, J. Ding, Small Methods **8**, 2400428 (2024)
14. X. Li, D. Bi, C. Yi, J.-D. Décoppet, J. Luo, S.M. Zakeeruddin, A. Hagfeldt, M. Grätzel, Science **353**, 58 (2016)
15. C. Zhang, A. Zhang, G. Zhang, Y. Fang, J. Cheng, L. Liang, J. Shi, Z. Li, T. Meng, D. Wang, Org. Electron. **111**, 106652 (2022)
16. International Labour Organization, (n.d.). https://chemicalsafety.ilo.org/dyn/icsc/showcard.display?p_card_id=0457&p_edit=&p_version=2&p_lang=en
17. T. Wu, J. Wu, Y. Tu, X. He, Z. Lan, M. Huang, J. Lin, J. Power Sources **365**, 1 (2017)

18. M. Degani, Q. An, M. Albaladejo-Siguan, Y.J. Hofstetter, C. Cho, F. Paulus, G. Grancini, Y. Vaynzof, Sci. Adv. **7**, 1 (2021)
19. Y. Zhang, S. Jang, I.-W. Hwang, Y.K. Jung, B.R. Lee, J.H. Kim, K.H. Kim, S.H. Park, ACS Appl. Mater. Interfaces **12**, 24827 (2020)
20. Y. Bai, S. Xiao, C. Hu, T. Zhang, X. Meng, H. Lin, Y. Yang, S. Yang, Adv. Energy Mater. **7**, 1 (2017)
21. P. Chen, Y. Bai, S. Wang, M. Lyu, J. Yun, L. Wang, Adv. Funct. Mater. **28**, 1 (2018)
22. H.-S. Yoo, N.-G. Park, Sol. Energy Mater. Sol. Cells **179**, 57 (2018)
23. M. Legrand, B. Bérenguier, T. Campos, D. Ory, J.-F. Guillemoles, EPJ Photovoltaics **14**, 40 (2023)
24. D. Yang, T. Sano, Y. Yaguchi, H. Sun, H. Sasabe, J. Kido, Adv. Funct. Mater. **29**, 1970074 (2019)
25. L. Ke, S. Luo, X. Ren, Y. Yuan, J. Phys. D. Appl. Phys. **54**, 163001 (2021)
26. H. Chen, Q. Guan, H. Yan, X. Cui, Z. Shu, Y. Cai, ACS Appl. Mater. Interfaces **15**, 32475 (2023)
27. Y. Feng, Y. Zhang, C. Duan, M. Zhao, J. Dai, Opt. Mater. Express **12**, 3262 (2022)
28. P. Chhillar, B.P. Dhamaniya, V. Dutta, S.K. Pathak, ACS Omega **4**, 11880 (2019)
29. U. Rau, Phys. Rev. B **76**, 085303 (2007)
30. F. Peña-Camargo, P. Caprioglio, F. Zu, E. Gutierrez-Partida, C.M. Wolff, K. Brinkmann, S. Albrecht, T. Riedl, N. Koch, D. Neher, M. Stolterfoht, ACS Energy Lett. **5**, 2728 (2020)
31. T.P.A. van der Pol, K. Datta, M.M. Wienk, R.A.J. Janssen, Adv. Opt. Mater. **10**, 1 (2022)
32. A. Bonadio, F.P. Sabino, A.L.M. Freitas, M.R. Felez, G.M. Dalpian, J.A. Souza, Inorg. Chem. **62**, 7533 (2023)
33. H. Kim, M. Pei, Y. Lee, A.A. Sutanto, S. Paek, V.I.E. Queloz, A.J. Huckaba, K.T. Cho, H.J. Yun, H. Yang, M.K. Nazeeruddin, Adv. Funct. Mater. **30**, 1 (2020)

Cite this article as: Toshimitsu Mochizuki, Shota Araki, Hidetaka Takato, Katsuto Tanahashi, Performance analysis of DMF-free perovskite solar cells with vacuum quenching, EPJ Photovoltaics **16**, 18 (2025), https://doi.org/10.1051/epjpv/2025002